Edinburgh Research Explorer

A Measurement of the Wind Speed on a Brown Dwarf

OPEN ACCESS

Title: A Measurement of the Wind Speed on a Brown Dwarf

Authors: Katelyn N. Allers,[1*] Johanna M. Vos,[2] Beth A. Biller,[3,4] Peter K. G. Williams[5,6]

Affiliations:

[1]Department of Physics and Astronomy, Bucknell University, Lewisburg, PA 17837-2029, USA

[2]Department of Astrophysics, American Museum of Natural History, New York, NY 10024-5102, USA

[3]Scottish Universities Physics Alliance, Institute for Astronomy, University of Edinburgh, Edinburgh EH9 3HJ, UK

[4]Centre for Exoplanet Science, University of Edinburgh, Edinburgh EH9 3FCD, UK

[5]Center for Astrophysics, Harvard & Smithsonian, Cambridge, MA 02138-1516, USA

[6]American Astronomical Society, Washington, DC 20006-1681, USA

[*]Corresponding Author; E-mail: katelynallers@gmail.com.

Abstract: Zonal (latitudinal) winds dominate the bulk flow of planetary atmospheres. For gas giant planets such as Jupiter, the motion of clouds can be compared with radio emissions from the magnetosphere, which is connected to the planet's interior, to determine the wind speed. In principle, this technique can be applied to brown dwarfs and/or directly-imaged exoplanets if periods can be determined for both the infrared and radio emissions. We apply this method to measure the wind speeds on the brown dwarf 2MASS J10475385+2124234. The difference between the radio period of 1.751-1.765 hours and infrared period of 1.741 ± 0.007 hours implies a strong wind (650 ± 310 m s^{-1}) proceeding eastward. This could be due to atmospheric jet streams and/or low frictional drag at the bottom of the atmosphere.

Main Text

Gas giant exoplanets and brown dwarfs (objects with masses of 13–72 times that of Jupiter) rotate on timescales of hours to days (*1–4*). If there are any inhomogeneous features at the top of their atmospheres, such as clouds, the rotational modulation causes quasi-periodic variability in their brightness. Photometric searches for periodic brightness modulations can therefore probe the rotational properties of these objects. Quasi-periodic near- and mid-IR variability is common in brown dwarfs of spectral types L and T (*2, 5*).

Within the Solar System, it is possible to observe the effects of rapid rotation on the atmospheric physics of the giant planets. Zonal winds, latitudinal flows resulting from rapid rotation and convection, dominate the bulk atmospheric flow of Jupiter (*6*). Models of the atmospheric dynamics of brown dwarfs and exoplanets incorporate the effects of rotation and zonal winds (*7–9*). These studies have shown that wind speeds and flow patterns are determined by the efficiency with which the atmosphere can radiatively cool and the coupling between the atmosphere and interior of the planet, among other atmospheric conditions.

Wind speeds have been measured for some hot, gas giant exoplanets using Doppler shifts in transit spectroscopy (*10*). This technique requires a tidally-locked planet (for which the rotation period and orbital period are equal) as well as high speed winds (several km s^{-1}) driven by heat redistribution from the highly-irradiated day side to the night side of the planet (*10*). These conditions are not typical for planetary-mass objects, particularly those with wide separations from their parent star or free-floating objects which are not gravitationally bound to a star.

Photometric variability studies of brown dwarfs and free-floating, planetary-mass objects have inferred the presence of zonal winds (*11, 12*). Changes in the rotational modulation of brightness of a highly variable brown dwarf over several months could be due to wind speeds of $\sim$45 m s^{-1} (*11*). Quasi-periodic variability data for two brown dwarfs has been modeled as originating from beating, planetary-scale, atmospheric wave pairs with differential wind velocities of several hundred m s^{-1} (*12*).

We describe an alternative technique for measuring wind speeds (v_{wind}) on exoplanets and brown dwarfs. Observations of Jupiter are typically interpreted using a coordinate system known as System III, whose rotation period is 9h 55m 30s, determined from Jupiter's radio emission (*13*). This radio periodicity corresponds to the rotation rate of Jupiter's magnetosphere. Because the Jovian magnetic field originates >7000 km below its visible surface (*14*), the radio period is determined by the rotation of interior of the planet, which is expected to rotate as a rigid body (*15*). An alternative coordinate system for Jupiter's surface features is known as System I, which has a period of 9h 50m 30s, measured from the rotation of its atmospheric features in optical and infrared light from 10° N to 10° S. This 5 minute difference between the radio System III period (T_{interior}) and optical/IR System I period ($T_{\mathrm{atmosphere}}$) corresponds to a velocity difference at the radius of Jupiter's visible surface ($R = 71,492$ km) of

$$v_{\mathrm{wind}} = 2\pi R \left(\frac{1}{T_{\mathrm{atmosphere}}} - \frac{1}{T_{\mathrm{interior}}} \right) = +106 \text{ m s}^{-1},$$
(1)

2

which agrees with the measured wind speed observed in Jupiter's equatorial region (*16*).

Radio observations of brown dwarfs have been used to measure the rotational modulation of their magnetic field (*17*), in some cases with uncertainties as low as 0.11 minutes. Radio emission detected from brown dwarfs originates from the same mechanism (electron-cyclotron maser instability, hereinafter ECMI) as Jupiter's radio emission, as shown by observations (*18*) and models (*19*). For brown dwarfs of spectral type L and T, the magnetic field is expected to originate well below the visible surface (*20*). Therefore, we expect the radio period of brown dwarfs and exoplanets to represent their interior period of rotation, as it does for Jupiter.

If global maps of Jupiter were degraded to unresolved photometric measurements (akin to those available for brown dwarfs), they would have variability amplitudes as large as 20% (*21*), which is similar to those seen in the most highly variable brown dwarfs (*3*). Optical/IR photometric monitoring of brown dwarfs can determine rotational periods with precisions <1 minute from the ground (*22*) or from space (*2*). Wind speed measurements of brown dwarfs and planetary-mass objects should therefore be possible by measuring radio and IR periods using current facilities.

We applied this method to observations of two brown dwarfs: 2MASS J10475385+2124234 (hereafter 2MASS J1047+21) and WISE J112254.73+255021.5 (hereafter WISE J1122+25). No infrared period was detected for WISE J1122+25 (*23*), so we focus our discussion on 2MASS J1047+21.

2MASS J1047+21 is a brown dwarf of spectral type T6.5 that lies 10.6 pc away (*24*). Based on its luminosity and evolutionary models for ages of 0.5–10 Gyr, 2MASS J1047+21 has an estimated mass of 16–68 times that of Jupiter and an estimated temperature of 880 ± 76 K (*24*). Circularly polarized bursts of radio emission have been detected from 2MASS J1047+21, consistent with ECMI and indicating a rotation period of 1.77 ± 0.04 hours (*25*) and a magnetic field strength of 5.6 kG (*26*).

We used the Infrared Array Camera on the Spitzer Space Telescope to search for photometric variability of 2MASS J1047+21 at 4.5 μm (*23*). Observations were conducted on 2017 April 07 for 7 hours and on 2018 April 15 for 14 hours. We detect sinusoidal variability (Figure 1) in both epochs with an amplitude of 0.5%, indicating that a single, long-lived atmospheric feature is likely responsible for the observed variability. We used two approaches to determine the IR period: a sinusoidal model fitted using Markov Chain Monte Carlo (MCMC), and an analysis of the Lomb-Scargle periodogram (Figure 2A) using bootstrap and Monte Carlo techniques for uncertainty determination (Figure 2B–C). The resulting periods and uncertainties agree with each other (*23*). We adopt an IR period of 1.741 ± 0.007 hours.

We also observed 2MASS J1047+21 at 4–8 GHz with the Karl G. Jansky Very Large Array (VLA) on the nights of 2018 October 12-14 (*23*). Our radio observations (Figure 3) show periodic, highly-circularly polarized bursts of ECMI emission, consistent with the previous observations (*25*). We determined the radio period using a time-of-arrival (TOA) analysis and an analysis of the Lomb-Scargle periodogram, which give consistent radio periods of 1.758 hours. The uncertainties calculated by bootstrap and Monte Carlo approaches are both very low, 0.0012 hours, which we interpret as an underestimate of the true uncertainty, because the

pulse profiles are highly variable. Taking a more conservative approach, we computed a range of plausible periods from the TOA of the first and last pulses and their pulse widths. This approach yields a period range of 1.751–1.765 hours. Folding the radio data by different periods (Figure 4) shows that pulses align in phase for periods in the range 1.751–1.765 hours, but are not well aligned for periods outside that range.

For an IR period of $T_{\mathrm{atmosphere}} = 1.741 \pm 0.007$ hours, a uniformly-distributed radio period of $T_{\mathrm{interior}} = 1.751 - 1.765$ hours, and a radius of 67,200 km (*24*), we determine a wind speed for 2MASS J1047+21 of 650 ± 310 m s^{-1}. Equation 1 assumes that the infrared variability originates in the equatorial region, but can be adapted to other latitudes by scaling by the cosine of the latitude. The inclination of 2MASS J1047+21's rotation is unknown, but all other radio-bursting brown dwarfs with known inclinations are viewed nearly equator-on (*18*). Photometric variability most commonly originates at equatorial to mid-latitudes of less than 35° (*21*, *27*). Thus, latitudinal or viewing-angle effects would likely change the result by less than the uncertainty. The measured wind speed is that of the (unknown) atmospheric inhomogeneity that dominates the photometric variability. If this atmospheric feature occurs between bands of zonal winds having alternating wind direction or is transported by a process other than wind (*28*), our measured wind speed could be an underestimate of the true zonal wind speed.

We detect a positive (eastward) wind speed at >98% confidence (2.1σ). As with Jupiter, the IR period of 2MASS J1047+21 is shorter than its radio period, indicating an atmosphere that is rotating faster than the interior. The wind speed on 2MASS J1047+21 is higher than on the gas giant planets in the Solar System (*16*, *29*). Analytic theory predicts that larger atmospheric heat fluxes lead to higher wind speeds (*7*). 3D numerical simulations show that zonal winds of hundreds of m s^{-1} can occur when strong convective forcing and/or weak damping (either radiative or frictional) promote the formation of atmospheric jet streams (*9*).

Recent work indicates hot Jupiters may have magnetic fields strengths of $\sim$100 G (*30*), weaker than the kG fields of brown dwarfs (*26*).

References

1. I. A. G. Snellen, B. R. Brandl, R. J. de Kok, M. Brogi, J. Birkby, H. Schwarz, Fast spin of the young extrasolar planet β Pictoris b. *Nature* **509**, 63–65 (2014).

2. S. A. Metchev *et al.*, Weather on Other Worlds. II. Survey Results: Spots are Ubiquitous on L and T Dwarfs. *Astrophys. J* **799**, 154 (2015).

3. B. A. Biller *et al.*, Simultaneous Multiwavelength Variability Characterization of the Free-floating Planetary-mass Object PSO J318.5-22. *Astron. J.* **155**, 95 (2018).

4. Y. Zhou *et al.*, Cloud Atlas: High-contrast Time-resolved Observations of Planetary-mass Companions. *Astron. J.* **157**, 128 (2019).

5. J. Radigan, D. Lafrenière, R. Jayawardhana, E. Artigau, Strong Brightness Variations Signal Cloudy-to-clear Transition of Brown Dwarfs. *Astrophys. J* **793**, 75 (2014).

6. Y. Kaspi *et al.*, Jupiter′s atmospheric jet streams extend thousands of kilometres deep. *Nature* **555**, 223–226 (2018).

7. A. P. Showman, Y. Kaspi, Atmospheric Dynamics of Brown Dwarfs and Directly Imaged Giant Planets. *Astrophys. J* **776**, 85 (2013).

8. G. Lee, C. Helling, I. Dobbs-Dixon, D. Juncher, Modelling the local and global cloud formation on HD 189733b. *Astron. & Astrophys.* **580**, A12 (2015).

9. A. P. Showman, X. Tan, X. Zhang, Atmospheric Circulation of Brown Dwarfs and Jupiter- and Saturn-like Planets: Zonal Jets, Long-term Variability, and QBO-type Oscillations. *Astrophys. J* **883**, 4 (2019).

10. T. Louden, P. J. Wheatley, Spatially Resolved Eastward Winds and Rotation of HD 189733b. *Astrophys. J. Lett.* **814**, L24 (2015).

11. J. Radigan, R. Jayawardhana, D. Lafrenière, É. Artigau, M. Marley, D. Saumon, Large-amplitude Variations of an L/T Transition Brown Dwarf: Multi-wavelength Observations of Patchy, High-contrast Cloud Features. *Astrophys. J* **750**, 105 (2012).

12. D. Apai *et al.*, Zones, spots, and planetary-scale waves beating in brown dwarf atmospheres. *Science* **357**, 683–687 (2017).

13. P. K. Seidelmann *et al.*, Report of the IAU/IAG Working Group on cartographic coordinates and rotational elements: 2006. *Celestial Mechanics and Dynamical Astronomy* **98**, 155–180 (2007).

14. C. A. Jones, A dynamo model of Jupiter's magnetic field. *Icarus* **241**, 148–159 (2014).

15. T. Guillot *et al.*, A suppression of differential rotation in Jupiter′s deep interior. *Nature* **555**, 227–230 (2018).

16. J. Tollefson *et al.*, Changes in Jupiter's Zonal Wind Profile preceding and during the Juno mission. *Icarus* **296**, 163–178 (2017).

17. E. Berger *et al.*, Periodic Radio and Hα Emission from the L Dwarf Binary 2MASSW J0746425+200032: Exploring the Magnetic Field Topology and Radius Of An L Dwarf. *Astrophys. J* **695**, 310–316 (2009).

18. G. Hallinan, A. Antonova, J. G. Doyle, S. Bourke, C. Lane, A. Golden, Confirmation of the Electron Cyclotron Maser Instability as the Dominant Source of Radio Emission from Very Low Mass Stars and Brown Dwarfs. *Astrophys. J* **684**, 644–653 (2008).

19. J. D. Nichols *et al.*, Origin of Electron Cyclotron Maser Induced Radio Emissions at Ultracool Dwarfs: Magnetosphere-Ionosphere Coupling Currents. *Astrophys. J* **760**, 59 (2012).

20. M. M. Kao *et al.*, Auroral Radio Emission from Late L and T Dwarfs: A New Constraint on Dynamo Theory in the Substellar Regime. *Astrophys. J* **818**, 24 (2016).

21. H. Ge *et al.*, Rotational Light Curves of Jupiter from Ultraviolet to Mid-infrared and Implications for Brown Dwarfs and Exoplanets. *Astron. J.* **157**, 89 (2019).

22. M. Gillon *et al.*, Fast-evolving weather for the coolest of our two new substellar neighbours. *Astron. & Astrophys.* **555**, L5 (2013).

23. K. N. Allers, Placeholder. *Supplmentary Materials*.

24. J. C. Filippazzo, E. L. Rice, J. Faherty, K. L. Cruz, M. M. Van Gordon, D. L. Looper, Fundamental Parameters and Spectral Energy Distributions of Young and Field Age Objects with Masses Spanning the Stellar to Planetary Regime. *Astrophys. J* **810**, 158 (2015).

25. P. K. G. Williams, E. Berger, The Rotation Period and Magnetic Field of the T Dwarf 2MASSI J1047539+212423 Measured from Periodic Radio Bursts. *Astrophys. J* **808**, 189 (2015).

26. M. M. Kao, G. Hallinan, J. S. Pineda, D. Stevenson, A. Burgasser, The Strongest Magnetic Fields on the Coolest Brown Dwarfs. *Astrophys. J. Supplement* **237**, 25 (2018).

27. J. M. Vos, K. N. Allers, B. A. Biller, The Viewing Geometry of Brown Dwarfs Influences Their Observed Colors and Variability Amplitudes. *Astrophys. J* **842**, 78 (2017).

28. D. S. Choi, A. P. Showman, A. R. Vasavada, A. A. Simon-Miller, Meteorology of Jupiter's equatorial hot spots and plumes from Cassini. *Icarus* **223**, 832–843 (2013).

29. E. García-Melendo, S. Pérez-Hoyos, A. Sánchez-Lavega, R. Hueso, Saturn's zonal wind profile in 2004-2009 from Cassini ISS images and its long-term variability. *Icarus* **215**, 62–74 (2011).

30. P. W. Cauley, E. L. Shkolnik, J. Llama, A. F. Lanza, Magnetic field strengths of hot Jupiters from signals of star-planet interactions. *Nature Astronomy*, 408 (2019).

31. K. N. Allers, Placeholder. *DOI for electronic materials*.

32. G. G. Fazio *et al.*, The Infrared Array Camera (IRAC) for the Spitzer Space Telescope. *Astrophys. J. Supplement* **154**, 10–17 (2004).

33. J. G. Ingalls *et al.*, "Intra-pixel gain variations and high-precision photometry with the Infrared Array Camera (IRAC)", in *Space Telescopes and Instrumentation 2012: Optical, Infrared, and Millimeter Wave*, ed. by M. C. Clampin, G. G. Fazio, H. A. MacEwen, J. M. O. Jr. (SPIE, 2012), vol. 8442, pp. 693–705.

34. P. J. Lowrance *et al.*, "Modifications to the warm Spitzer data reduction pipeline", in *Space Telescopes and Instrumentation 2012: Optical, Infrared, and Millimeter Wave*, ed. by M. C. Clampin, G. G. Fazio, H. A. MacEwen, J. M. O. Jr. (SPIE, 2012), vol. 8442, pp. 1150–1158.

35. M. C. Cushing *et al.*, The First Detection of Photometric Variability in a Y Dwarf: WISE J140518.39+553421.3. *Astrophys. J* **823**, 152 (2016).

36. M. G. Kendall, A New Measure of Rank Correlation. *Biometrika* **30**, 81–93 (1938).

37. H. A. Knutson, D. Charbonneau, L. E. Allen, A. Burrows, S. T. Megeath, The 3.6-8.0 μm Broadband Emission Spectrum of HD 209458b: Evidence for an Atmospheric Temperature Inversion. *Astrophys. J* **673**, 526–531 (2008).

38. A. N. Heinze *et al.*, Weather on Other Worlds. I. Detection of Periodic Variability in the L3 Dwarf DENIS-P J1058.7-1548 with Precise Multi-wavelength Photometry. *Astrophys. J* **767**, 173 (2013).

39. J. L. Hora *et al.*, "The IRAC point response function in the warm Spitzer mission", in *Space Telescopes and Instrumentation 2012: Optical, Infrared, and Millimeter Wave*, ed. by M. C. Clampin, G. G. Fazio, H. A. MacEwen, J. M. O. Jr. (SPIE, 2012), vol. 8442, pp. 1159–1164.

40. J. M. Vos *et al.*, Variability of the lowest mass objects in the AB Doradus moving group. *Mon. Not. R. Astron. Soc.* **474**, 1041–1053 (2018).

41. N. R. Lomb, Least-Squares Frequency Analysis of Unequally Spaced Data. *Astrophysics and Space Science* **39**, 447–462 (1976).

42. J. D. Scargle, Studies in astronomical time series analysis. II. Statistical aspects of spectral analysis of unevenly spaced data. *Astrophys. J* **263**, 835–853 (1982).

43. D. Foreman-Mackey, D. W. Hogg, D. Lang, J. Goodman, emcee: The MCMC Hammer. *Publ. Astron. Soc. Pac.* **125**, 306 (2013).

44. J. T. VanderPlas, Understanding the Lomb-Scargle Periodogram. *Astrophys. J. Supplement* **236**, 16 (2018).

45. J. P. McMullin, B. Waters, D. Schiebel, W. Young, K. Golap, "CASA Architecture and Applications", in *Astronomical Data Analysis Software and Systems XVI*, ed. by R. A. Shaw, F. Hill, D. J. Bell (Astronomical Society of the Pacific Conference Series, 2007), vol. 376, p. 127.

46. A. R. Offringa, A. G. de Bruyn, M. Biehl, S. Zaroubi, G. Bernardi, V. N. Pandey, Post-correlation radio frequency interference classification methods. *Mon. Not. R. Astron. Soc.* **405**, 155–167 (2010).

47. A. R. Offringa, J. J. van de Gronde, J. B. T. M. Roerdink, A morphological algorithm for improving radio-frequency interference detection. *Astron. & Astrophys.* **539**, A95 (2012).

48. J. E. Noordam, "LOFAR calibration challenges", in *Ground-based Telescopes*, ed. by J. M. O. Jr. (SPIE, 2004), vol. 5489, pp. 817–825.

49. H. T. Intema, S. van der Tol, W. D. Cotton, A. S. Cohen, I. M. van Bemmel, H. J. A. Röttgering, Ionospheric calibration of low frequency radio interferometric observations using the peeling scheme. I. Method description and first results. *Astron. & Astrophys.* **501**, 1185–1205 (2009).

50. P. K. G. Williams, K. N. Allers, B. A. Biller, J. Vos, A Tool and Workflow for Radio Astronomical Peeling in CASA. *Res. Notes AAS* **3**, 110 (2019).

51. R. J. Sault, M. H. Wieringa, Multi-frequency synthesis techniques in radio interferometric imaging. *Astron. & Astrophys. Supp.* **108**, 585–594 (1994).

52. T. J. Cornwell, K. Golap, S. Bhatnagar, "W Projection: A New Algorithm for Wide Field Imaging with Radio Synthesis Arrays", in *Astronomical Data Analysis Software and Systems XIV*, ed. by P. Shopbell, M. Britton, R. Ebert (Astronomical Society of the Pacific Conference Series, 2005), vol. 347, p. 86.

53. P. K. G. Williams, E. Berger, B. A. Zauderer, Quasi-quiescent Radio Emission from the First Radio-emitting T Dwarf. *Astrophys. J. Lett.* **767**, L30 (2013).

54. W. Sieber, R. Reinecke, R. Wielebinski, Observations of pulsars at high frequencies. *Astron. & Astrophys.* **38**, 169–182 (1975).

55. T. Karalidi, D. Apai, G. Schneider, J. R. Hanson, J. M. Pasachoff, Aeolus: A Markov Chain Monte Carlo Code for Mapping Ultracool Atmospheres. An Application on Jupiter and Brown Dwarf HST Light Curves. *Astrophys. J* **814**, 65 (2015).

56. E. Buenzli *et al.*, Vertical Atmospheric Structure in a Variable Brown Dwarf: Pressure-dependent Phase Shifts in Simultaneous Hubble Space Telescope-Spitzer Light Curves. *Astrophys. J. Lett.* **760**, L31 (2012).

57. H. Yang *et al.*, Extrasolar Storms: Pressure-dependent Changes in Light-curve Phase in Brown Dwarfs from Simultaneous HST and Spitzer Observations. *Astrophys. J* **826**, 8 (2016).

58. E. Manjavacas *et al.*, Cloud Atlas: Rotational Spectral Modulations and Potential Sulfide Clouds in the Planetary-mass, Late T-type Companion Ross 458C. *Astrophys. J. Lett.* **875**, L15 (2019).

Acknowledgments

data using Lomb-Scargle periodograms with various uncertainty determinations and wrote the introduction to the manuscript. PW planned, proposed for, and reduced the VLA data, conducted the TOA analysis and figure creation, and wrote the corresponding text. **Competing interests:** none. **Data and materials availability:** All VLA data are available via the NRAO Science Data Archive under Project Code 18A-427. All Spitzer data are available via the Spitzer Heritage Archive using Program IDs 13031 and 13231. (*31*)

Supplementary materials

Materials and Methods
Supplementary Text
Tables S1-S3
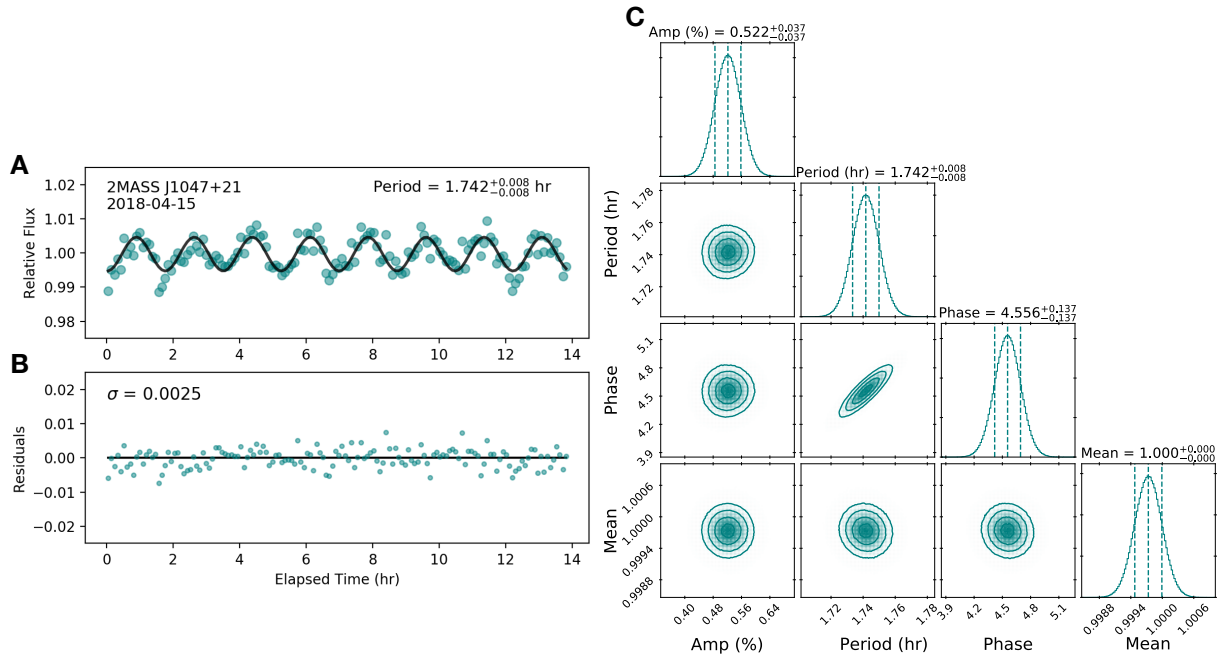Figs. S1 to S6
References (*31-57*)

Fig. 1. Spitzer photometry of 2MASS J1047+21 on 2018 April 15 and our MCMC analysis. (A) Photometry in 5.5-minute bins at 4.5 μm (points) and the fitted sinusoidal model (black curve). (B) The residuals between the model and observations. The residuals are consistent with Gaussian-distributed noise. (C) Posterior probability distributions for the model parameters. "Amp" refers to the semi-amplitude of the sinusoidal model. The mean refers to the average relative flux of our target. Vertical dashed lines show the median and 1σ uncertainties on the best-fit parameters, which are defined by the 16% and 84% quantiles of the distributions. Contours show the 0.5, 1.0, 1.5, and 2.0-σ uncertainties for posteriors of each two-dimensional parameter space.

10
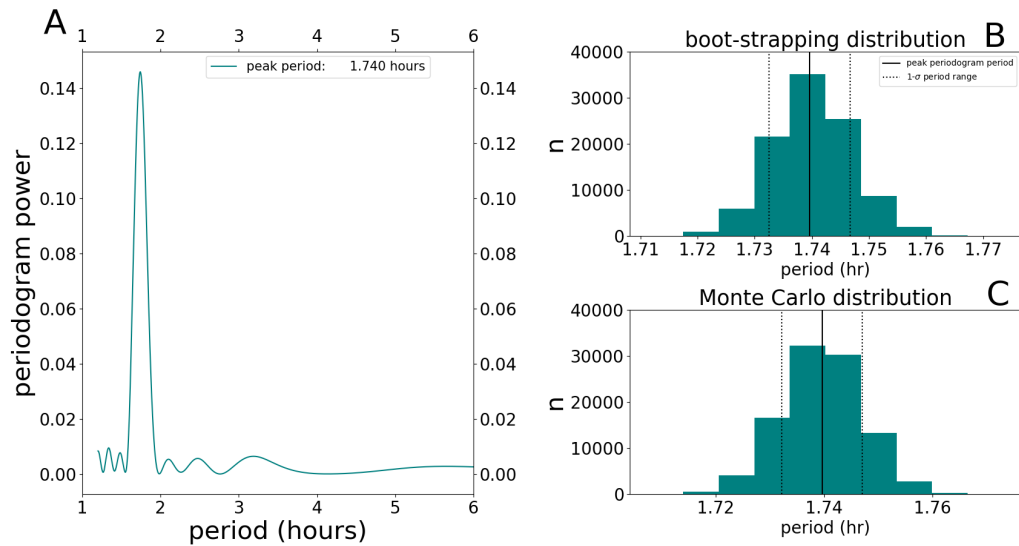
Fig. 2. Lomb-Scargle periodogram analysis of Spitzer photometry on 2018 April 15. (A) Periodogram showing an estimate of the Fourier power as a function of rotation perion. The highest-power period is 1.740 hours. (B) Distribution of retrieved highest-power periods from boot-strapping and (C) Monte Carlo methods. The solid vertical lines show the median of the distribution and the dotted vertical lines show the 1σ uncertainties. Both methods indicate an uncertainty of 0.007 hours.
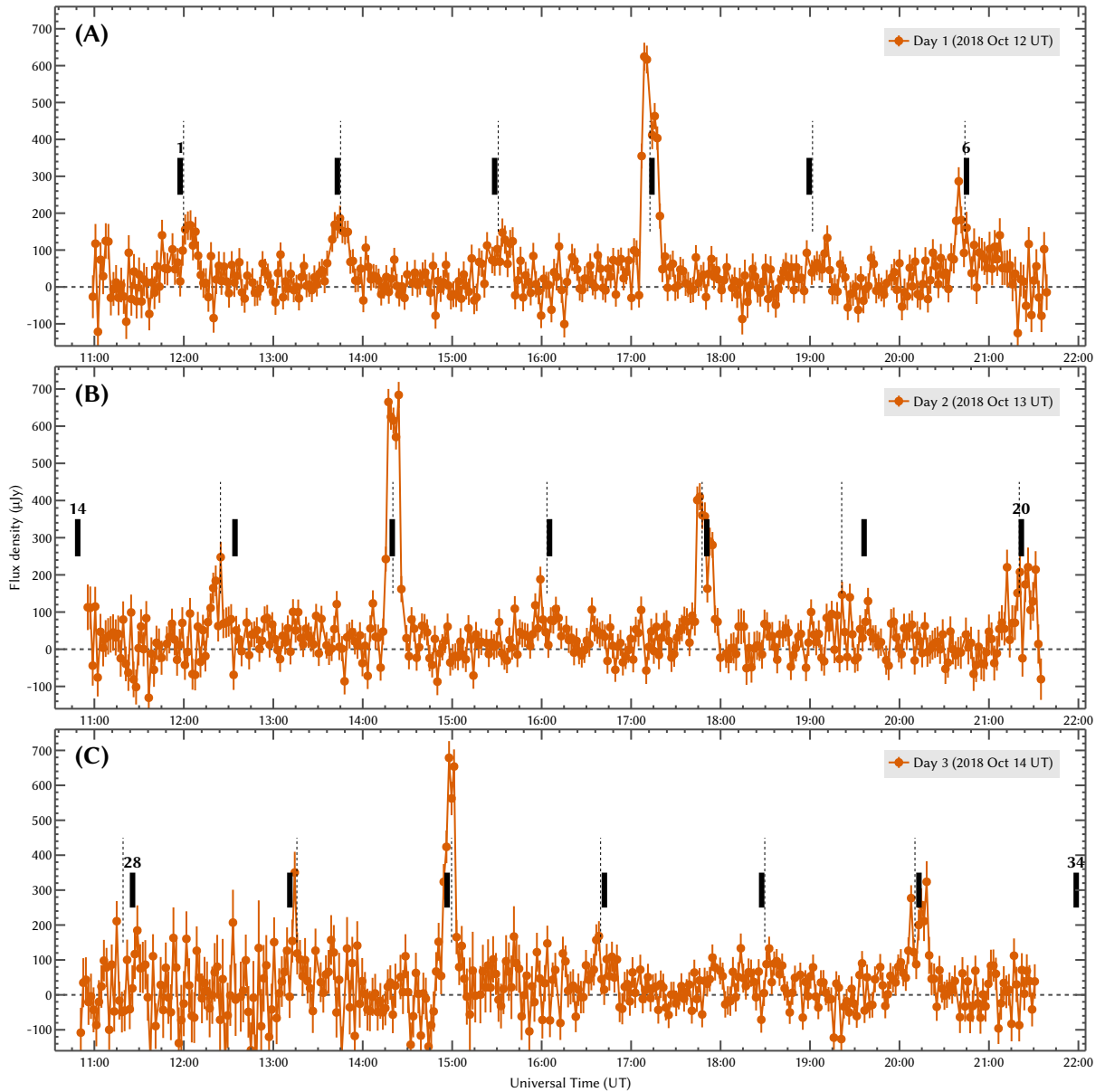
Fig. 3. Radio light curve of 2MASS J1047+21 from VLA observations. (A-C) Left circularly-polarized radio flux in microjanskys (points) on three consecutive nights of observations, each lasting about 10 hours. 1σ uncertainties are plotted as vertical lines for each data point. Radio pulses of varying intensity are evident. Thin vertical dashed lines indicate pulse TOAs (*23*). Thick vertical solid lines indicate TOAs from the best-fitting period derived from these data, labelled with the number of rotations since the start of the observation. The data cover about 18 rotations out of 34 that occurred in this period.
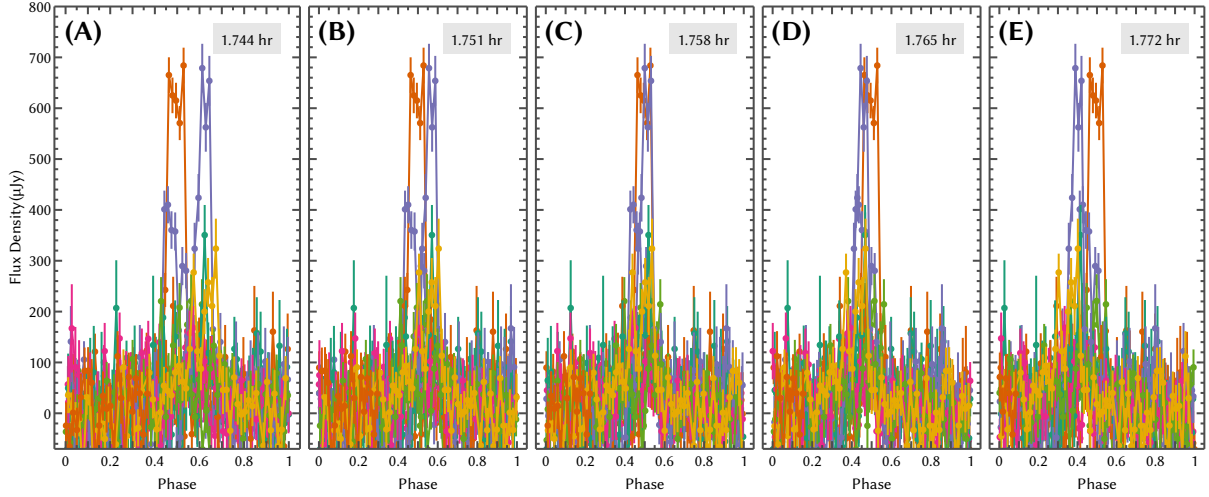
Fig. 4. Alignment of pulses for possible periods of the radio data. (A-E) The data (points) are folded by periods that differ by 0.007 hours for comparison of the phase of radio pulses. Each color indicates the data from a separate rotation. (C) Shows the radio pulses folded at the period preferred by our analysis (*23*). At this period, the pulses from all of our observed rotations are aligned at a phase of around 0.5. We consider periods in the range 1.751–1.765 hours to be plausible.

Materials and Methods

Spitzer Infrared Photometry

Observations and Data Reduction

We used IRAC, the Infrared Array Camera (*32*), to search for IR variability at 4.5 μm in two known radio variable targets, 2MASS J1047+21 (right ascension $\alpha = 10^h47^m53.85^s$, declination $\delta = +21°24'23.5''$, equinox J2000) and WISE J1122+25 ($\alpha = 11^h22^m55.50^s, \delta = +25°50'25.1''$ J2000). The observations were carried out following the recommendations for obtaining high precision photometry from the Spitzer Science Center (*33*), using 30 sec exposures. The science targets were placed on a well-characterized part of the detector (Figure S1) to minimize correlated noise. The dates and times of our IRAC observations are available in Table S1.

We obtained photometry from the Basic Calibrated Data (BCD) images produced by the Spitzer Science Center pipeline version S19.2 (*34*). Photometric centroids of our target and reference sources were found using the BOX_CENTROIDER.PRO routine. Aperture photometry was performed on the target and stars using circular apertures with radii of $2.0 - 4.0$ pixels, in steps of 0.1. Because the apertures are small the intersection of the circular aperture with a square pixel was computed exactly, rather than using the default polygon approximation (*35*). Outliers were identified and rejected from the raw light curves using a 6σ clip. For each data set, we chose the aperture that produced the lowest rms light curve (Table S1) for the following analysis.

IRAC photometry is known to exhibit a systematic effect due to intra-pixel gain variations (*33*). Figure S2 A-B shows that the raw photometry is highly correlated with the x and y sub-pixel coordinates. We quantified the strength of correlation using Kendall's τ (*36*). We modeled the pixel phase effect as a function of the source position, as in previous studies (*37, 38*), using the cubic function:

$$f(x,y) = P_0 + P_1x + P_2y + P_3xy + P_4x^2 + P_5y^2 + P_6x^3 + P_7y^3 + P_8x^2y + P_9xy^2 \quad \text{(S1)}$$

where $f(x,y)$ represents the measured flux, P_i are the fitted coefficients, and x and y are the sub-pixel coordinates. We found that this correction decreases the correlation between the x and y sub-pixel coordinates and the flux, as seen in Figure S2 C-D and measured by Kendall's τ coefficient.

We also extracted photometry using Point Response Function (PRF) fitting using PRFs created for Spitzer (*39*). The PRF combines information on the optical properties of the telescope, the detector sampling, and intra-pixel gain variations. The obtained light curves were consistent with those obtained from aperture photometry, but had slightly higher photometric noise. For this reason we used the light curves obtained from aperture photometry for the remaining analysis.

We estimated the uncertainty of the photometric points by measuring the "point-to-point" noise (*5*). The standard deviation provides a measurement of noise for a flat light curve, and

thus includes both the noise and intrinsic variations of a periodic light curve. We therefore measured the point-to-point noise, defined as the standard deviation of the light curve subtracted from a shifted version of itself, divided by $\sqrt{2}$. This measurement of the noise is not sensitive to low frequency trends and can estimate the noise for both variable and non-variable targets. We additionally determined the photometric uncertainty from the uncertainty images provided by the Spitzer Science Center. We performed aperture photometry on the square of the uncertainty images, then calculated the square root to produce an estimate of the photometric noise. The result is consistent with the point-to-point noise, described above.

Identification of Variables

We identified variability using a periodogram analysis (*40*). We calculated the Lomb-Scargle periodograms (*41*, *42*) of our targets and reference sources (Figure S1) to determine the significance of trends in their light curves. We calculated the 1% false-alarm probability from 1000 simulated light curves created by randomly rearranging the times of photometric points from each reference star's light curve. Figure S3 A&C show the light curve and periodogram of WISE J1122+25. The periodogram shows no power above the 95% and 99% confidence thresholds, thus WISE J1122+25 does not show significant photometric variability above the noise. From our epoch 1 data of 2MASS J1047+21 (Figure S3 B&D), the periodogram shows power above the 99% confidence threshold, indicating detection of significant periodic variability for 2MASS J1047+21. Following this initial variability search, we obtained additional Spitzer observations of 2MASS J1047+21 (described above) to better determine its IR period.

Infrared Period Determination: Sinusoidal Model

We adopted two methods to measure the rotation period of 2MASS J1047+21 from the Spitzer light curve – a sinusoidal model using MCMC, and a periodogram analysis.

The light curve of 2MASS J1047+21 is stable over many rotations in both epochs, which is well-approximated by a sine function. We used MCMC to fit a sine curve to the data because this method produces robust uncertainties on the parameters. We performed the MCMC fitting on the first epoch, second epoch, and both epochs together. We used the EMCEE package (*43*) with 1000 walkers with 8000 steps, and then discarded a burn-in sample of 500 steps to obtain the posterior probability distribution for each parameter of the sinusoidal model.

Figure S4C and Figure 1C show the posterior probability distributions of the parameters for the sinusoidal model fit to each epoch of 2MASS J1047+21 data. The MCMC model fitting to the 7 hr, first epoch observation (2017 April 7) gives a period of 1.77 ± 0.03 hr (Figure S4). For the 14 hr, second epoch observation (2018 April 15), the best-fitting period is 1.742 ± 0.008 hr (Figure 1). The second epoch measurement has a lower uncertainty than the first epoch measurement due to a longer observing duration, but both period measurements and light curve amplitudes are consistent.

We also used MCMC to model sinusoidal variability for both epochs simultaneously. In this case we included an additional parameter, a phase offset for the first epoch of data. This phase offset is necessary for the fitting to converge, but is not physically meaningful, as our

period uncertainty is equivalent to more than a 2π phase offset between the two epochs. The posterior probability distributions of the parameters shown in Figure S5 are single-peaked and normally-distributed, with a best fitting period of $1.743^{+0.007}_{-0.008}$ hours. Fitting both epochs simultaneously provides little improvement in the period measurement, likely due to the time gap between epochs being too large to allow for robust phasing of the data. Table S2 provides a summary of the parameters of the sinusoidal model fit for our Spitzer datasets.

Infrared Period Determination: Periodogram

In addition to our MCMC period determination, we calculated the Lomb-Scargle periodogram for the second epoch Spitzer observation of 2MASS J1047+21. The Lomb-Scargle periodogram robustly shows a period of 1.7396 hours for the Spitzer light curve of 2MASS J1047+21 (see Figure 2). However, uncertainties are not easily estimated from the Lomb-Scargle periodogram itself (*44*).

We utilized two methods to estimate the uncertainty of this period: i) bootstrapping with replacement and ii) Monte-Carlo exploration of the uncertainties on our light curve. For the bootstrapping method, we produced 10^5 resampled iterations of the dataset, where each element of each resampled dataset is a randomly chosen element of the original dataset. The highest likelihood period for each resampled dataset was then determined from its Lomb-Scargle periodogram, with the adopted period and uncertainty on the period taken from the median and standard deviation of the resulting distribution of peak periodogram periods. We find a period of 1.740±0.007 hours via this method.

For the Monte-Carlo exploration, 10^5 iterations of the dataset were produced by generating an array of random numbers from a normal distribution with the same number of data elements as the original dataset, multiplying that array by the uncertainties on the original dataset, then generating a simulated dataset by adding the original dataset to the randomly-sampled error array. The highest likelihood period for each simulated dataset was then determined from its Lomb-Scargle periodogram, and the adopted period and uncertainty were taken from the median and standard deviation of the resulting distribution of peak periodogram periods. We find a period of 1.740±0.007 hours via this method. Both of these methods produce results consistent with each other and the MCMC sinusoidal model fitting.

Table S1 provides a summary of our period determinations from multiple analysis techniques, which are consistent. We adopt the mean period and mean uncertainty from these methods, 1.741±0.007 hr, as the infrared photometric period of 2MASS J1047+21.

Very Large Array Radio Data

VLA Observations and Data Reduction

We observed 2MASS J1047+21 with the VLA on the nights of 2018 October 12-14 UT. Each night's observations lasted for 11 hr, so the total time elapsed between the beginning of the first observation and the end of the last observation was 59 hr. The array was in its most compact "D" configuration. The standard "C band" wideband continuum mode was used, with

the observing frequencies covering the range 4–8 GHz with two basebands of 2.048 GHz width having 1024 spectral channels. Each night, the flux density and bandpass calibrator was the radio galaxy, 3C 286, and the phase calibrator was the quasar, 4C 21.28.

We analyzed the data using standard techniques inside the CASA software system (*45*). We flagged radio-frequency interference (RFI) automatically using the AOFLAGGER package (*46, 47*). Our initial analysis revealed that the sidelobes of bright, off-axis sources in the target field led to spurious signals in the light curve of 2MASS J1047+21 because the standard direction-independent calibration procedure did not fully capture the time-varying instrumental response to these sources. Before imaging the data we therefore applied a "peeling" operation (*48, 49*) in which we determined direction-dependent calibration terms towards these sources and subtracted them from the fringe visibilities (*50*).

Once the data were calibrated, we imaged and deconvolved them using multi-frequency synthesis (MFS) with two Taylor terms (*51*) and w-projection (*52*) with 128 planes. The final images used a cell size of $2''$ square and were 1801 pixels on a side. The full width at half maximum of the synthesized beam was $11'' \times 10''$ at a position angle of -19°, East from North. After the peeling of the bright off-axis sources as described above, the root-mean-squared residual at the center of the combined (three-night) image was 1.9 μJy. In this image, there is a point source at a position of $\alpha = 10^h47^m51.1^s, \delta = +21°24'08''$ (J2000) that we identify as 2MASS J1047+21. The positional uncertainty is $\sim4''$. The source's flux density in the image is 74 ± 9 μJy, which averages over both the source's temporal variability and its spectral structure over the wide (4–8 GHz) bandwidth of the MFS image.

We produced a visibility-domain model of all emission in the field besides 2MASS J1047+21 by using the CASA ft task on copies of the MFS Taylor-term images with 12×12 boxes of pixels around 2MASS J1047+21 set to zero. Subtracting this model from the visibility data leaves a residual containing only the contributions of 2MASS J1047+21 and any imperfections due to the data analysis procedure. We then generated complex dynamic spectra of 2MASS J1047+21 in the LL and RR (left and right circular, respectively) polarization products (*53*). We examined the total-intensity dynamic spectrum ($I^2 = LL^2 + RR^2$) visually and flagged a small number of time and frequency slots that were affected by residual RFI. The remaining unflagged data showed evidence for flaring time variability in the LL polarization product, consistent with previous studies (*25*). While there were hints of spectral structure in the data in the brightest flares, the S/N was insufficient to analyze the frequency dependence of the source's emission, so we averaged the dynamic spectrum in frequency to yield a time series. The real component of the LL time series is shown in Figure 3. The RR time series shows no compelling evidence of variability, indicating that the flares consist of strongly left-circular-polarized emission. The imaginary parts are consistent with noise, suggesting there are no major calibration artifacts.

Radio Period estimation

Visual inspection of Figure 3 suggests a characteristic timescale in the radio emission of 2MASS J1047+21, however the highly variable pulse profiles complicate the numerical analysis. Not enough is known about the radio pulses of brown dwarfs and the origin of their

5

variability to provide a statistical characterization of their behavior or to construct a predictive model. We cannot discern any patterns in pulse width, height, asymmetry, or spectral structure. This is similar to the radio emissions from pulsars, where radio pulses that are individually highly variable follow persistent underlying patterns — but individual pulsar observations typically cover thousands if not millions of pulses (*54*), compared to the ∼18 presented here.

Radio Periodogram Analysis

Similar to our analysis of the IR data, we used a Lomb-Scargle periodogram to determine the peak power period from our VLA timeseries. This yields a period of 1.7580 hours, but as before, uncertainties cannot be derived directly from the Lomb-Scargle periodogram itself. We repeated the boot-strapping and Monte Carlo analysis described above for the full 3-night VLA time-series. Results are presented in Figure S5. This yielded periods and uncertainties of 1.7580±0.0013 hr from bootstrapping and 1.7580±0.0012 hr from the MC method respectively.

Radio TOA-based analysis

We also performed a periodicity analysis based on pulse times-of-arrival. In this approach, we assumed the radio emission of 2MASS J1047+21 consists of discrete radio bursts that are perfectly periodic. For each pulse, a TOA can be measured, but the varying pulse profiles and amplitudes induce a random jitter on each TOA measurement that may exceed the scatter that would be achieved if each pulse had a uniform, high-S/N profile.

We begin with a manually-chosen pulse ephemeris with a period of 1.76 hr, derived from visual inspection of the data. Using this ephemeris, we calculate refined TOAs using the following method. For each pulse, we isolate a window centered on the pulse whose width is 60% of the period. We divide each window into two subsets: the "inner" part, centered on the pulse and having half the total width of the window, and the non-contiguous "outer" part, comprised of the remaining wings. The weighted average flux density in the outer part defines a baseline value that is subtracted from the data. The refined TOA is then defined as the time centroid of the baseline-subtracted flux measurements. The second-moment time centroid defines a representative pulse width:

$$W_n = \sqrt{\frac{\sum_i (t_i - \mathrm{TOA}_n)^2 S_i w_i}{\sum_i S_i w_i}}, \tag{S2}$$

where S_i is the i'th baseline-subtracted flux density measurement in the n'th window, $w_i = \sigma_i^{-2}$ is its weight, and t_i is its timestamp. These TOAs are shown in Figure 3.

To determine a period, we fitted a weighted linear model to the TOAs, after discarding events with negligible flux, namely pulse numbers 19, 28, and 32. The remaining pulses were weighted according to their total flux above the local baseline. This method yields a period of 1.758 hr, identical to the period determined from a Lomb-Scargle periodgram of our radio data. This best-fitting ephemeris is shown in Figure 3. The nominal uncertainty on the period computed from the weighted linear fit is 0.0012 hr, which is consistent with the uncertainties determined from periodogram analysis of our radio data.

6

We investigated several methods for quantifying the uncertainty on this measurement. Generally speaking, "formal" methods based on simple models of the data substantially underestimate the uncertainty. For instance, different phasings varying by 0.0012 hr are equally acceptable to the human eye.

For continuous observations of a periodic signal, the uncertainty on the period measurement is inversely proportional to the time baseline of the observation (*44*). Therefore we choose to quantify the uncertainty by computing bracketing periods from the first and last TOAs and their characteristic pulse widths:

$$P_{\pm} = \frac{(\mathrm{TOA}_{33} \pm W_{33}) - (\mathrm{TOA}_1 \mp W_1)}{33 - 1}, \tag{S3}$$

This procedure yields a period range of $1.751 - 1.765$ hr. Visually, this range seems appropriate in that phasings of the data within this period range appear plausible (Figure 4) while those outside of this range are inferior.

In summary, our TOA approach yields a period measurement that can be characterized as having a value of $1.751 - 1.765$ hr. This is consistent with the previously reported radio period of $1.73 - 1.81$ hr (*25*). We repeated our analysis with variations in choices such as the TOA window width, weighting scheme, and number of iterations in the TOA determination process; the results are all consistent with the range reported here. Our reported uncertainty is not Gaussian, nor is it derived in any formally rigorous manner.

Supplementary Text

Long-term Spitzer Light Curve Stability

The Spitzer light curve of 2MASS J1047+21 appears stable over the two observed epochs, over a year apart. In both epochs, the observed light curves are well fitted by a single sinusoidal model with consistent amplitudes of 0.5%. The sinusoidal nature of the variability suggests either a planetary-scale modulated band (*12*) or perhaps two features separated by $\sim$180 degrees of longitude, one of which causes peaks and the other troughs (*55*). Though many brown dwarfs exhibit rapid light curve evolution (*12*), the stability seen in the light curve of 2MASS J1047+21 is similar to that observed in 2MASS J22282889$-$431026, another T6.5 brown dwarf with observations spanning multiple years (*2*, *56*, *57*). Likewise, the late T dwarfs 2MASS J00501194$-$3322402 (spectral type T7) and Ross 458C (spectral type T8) exhibit variability that is well fitted by single sinusoidal models (*2*, *58*). Thus, sinusoidal variability driven by long-lived atmospheric inhomogeneities may well be typical among late-T dwarfs.

Table S1. Summary of observations

Target	Date (UT)	Time (UT)	Aperture Radius (pixels)
WISE J1122+25	2017 April 6	01:22:11 to 09:08:13	2.6
2MASS J1047+21	2017 April 7	18:29:56 to 01:24:08	2.4
2MASS J1047+21	2018 April 15	03:38:09 to 17:27:01	2.7

Table S2. Best fit parameters of our MCMC model fitting for 2MASS J1047+21

Date	2017 April 7	2018 April 15	Both epochs
Amplitude (%)	0.512 ± 0.047	0.522 ± 0.037	$0.496^{+0.027}_{-0.028}$
Period (hr)	$1.767^{+0.027}_{-0.025}$	1.742 ± 0.008	$1.743^{+0.007}_{-0.008}$
Phase (radians)	0.28 ± 0.12	4.56 ± 0.14	-1.66 ± 0.13
Mean Flux	1.001	1.000	1.000
Offset (radians)	$\cdots$	$\cdots$	$1.77^{+0.13}_{-0.14}$

Table S3. Summary of period determinations

| **Spitzer** 4.5 μ**m photometry**	Period (hr)
MCMC of Epoch 2	1.742 ± 0.008
MCMC of Epochs 1 & 2	$1.743^{+0.007}_{-0.008}$
Periodogram of Epoch 2 with bootstrap uncertainty	1.740 ± 0.007
Periodogram of Epoch 2 with MC uncertainty	1.740 ± 0.007
Adopted Infrared Period	1.741 ± 0.007
VLA 4-8 GHz LL **polarization flux**	Period (hr)
Periodogram with bootstrap uncertainty	1.7580 ± 0.0013
Periodogram with MC uncertainty	1.7580 ± 0.0012
Weighted Linear Fit to TOAs	1.7580 ± 0.0012
Bracketing TOAs	$1.751 - 1.765$
Adopted Radio Period	$1.751 - 1.765$
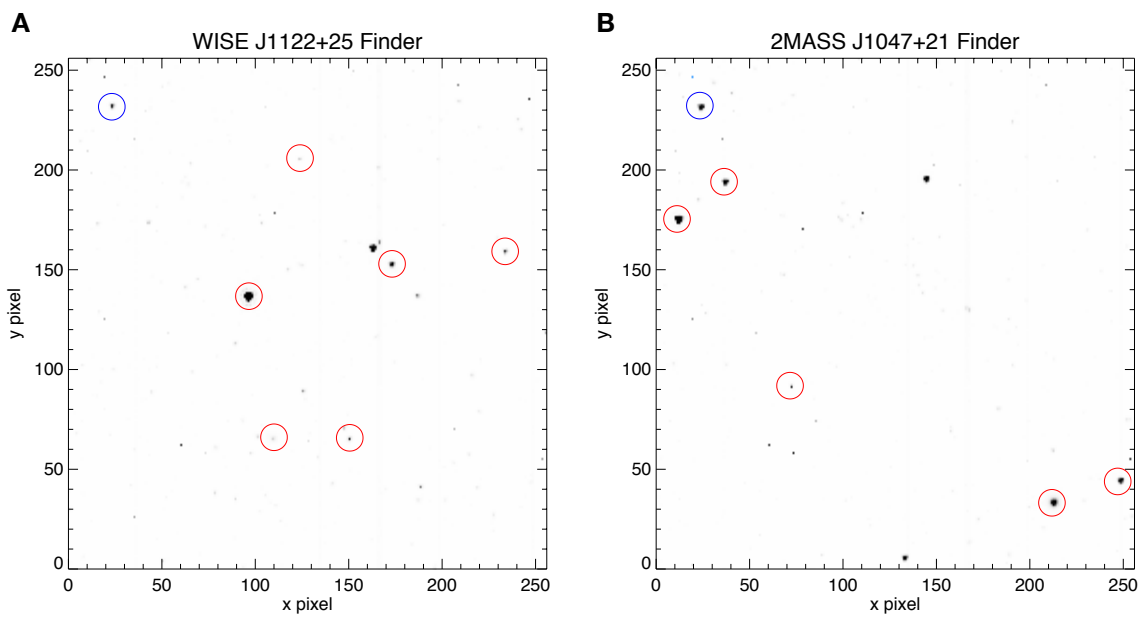
Fig. S1. IRAC images of WISE J1122+25 (A) and 2MASS J1047+21 (B). Targets are circled in blue. The reference stars used for periodogram analysis are circled in red.
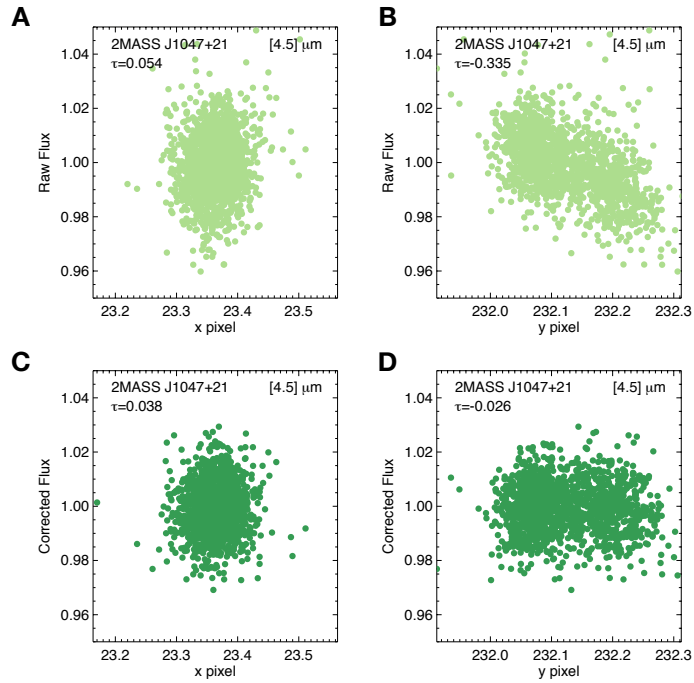
Fig. S2. Spitzer intrapixel sensitivity variations and correction. Raw Spitzer/IRAC photometry obtained from aperture photometry is correlated with x and y sub-pixel positions. We correct for this by fitting a cubic function of the source position. A-B show the correlation between the raw flux and pixel position. C-D show the corrected flux plotted against pixel position. Kendall's τ coefficient is a measure of the significance of correlation between two values – in all cases Kendall's τ coefficient decreases after pixel phase correction.
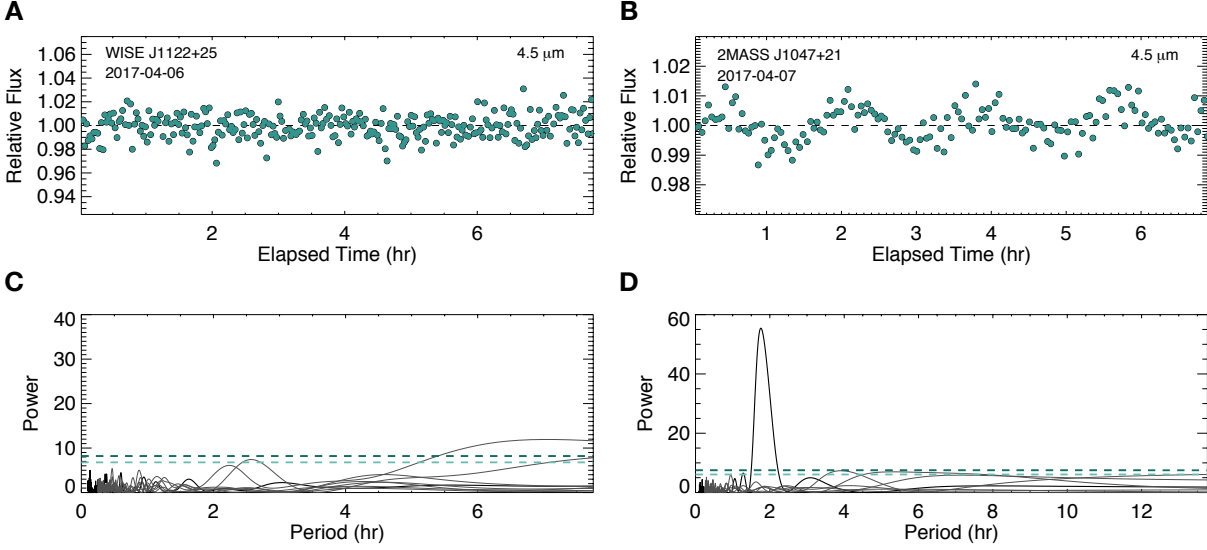
Fig. S3. Identification of Spitzer variability. Binned Spitzer 4.5 μm light curves of WISE J1122+25 (A) and epoch 1 data of 2MASS J1047+21 (B). C-D Periodograms of WISE J1122+25 and 2MASS J1047+21 are shown in black and reference stars in the field of view are shown in grey. The 95% and 99% significance thresholds are shown by the dashed green and blue lines, respectively. WISE J1122+25 does not show photometric variability above the noise. 2MASS J1047+21 shows significant variability and was thus chosen for additional follow up.
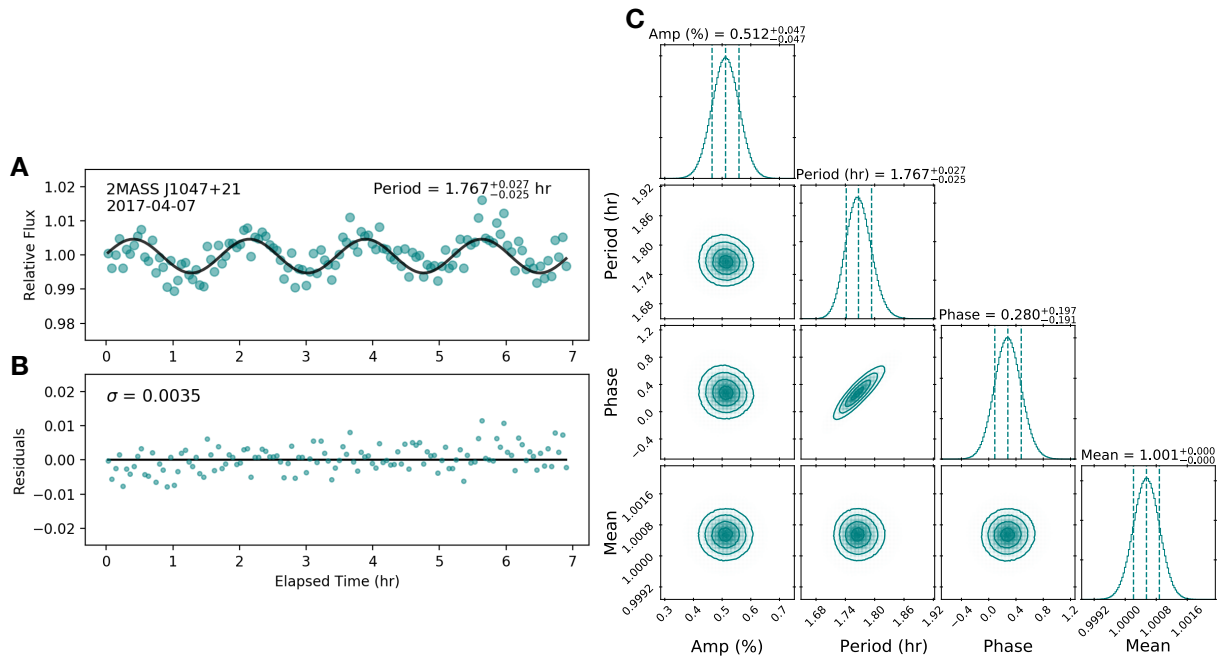
11

Fig. S4. MCMC analysis of our 2017 April 7 Spitzer 4.5 μm photometry. Same as Figure 1, but for the first epoch Spitzer observations of 2MASS J1047+21.
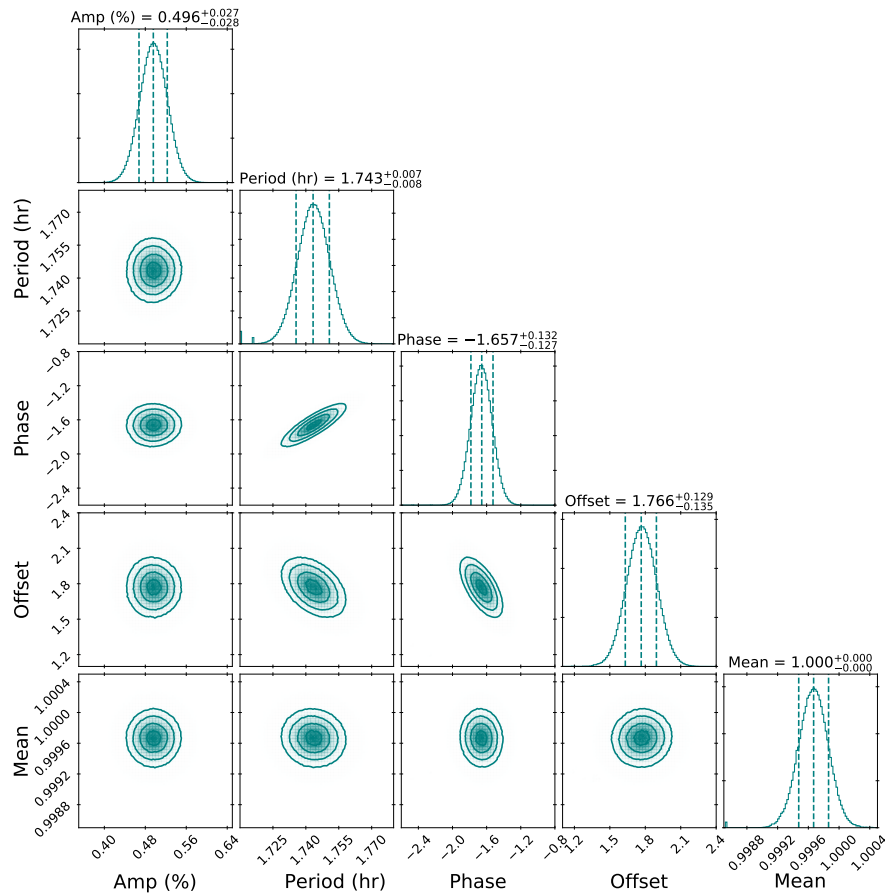
Fig. S5. Posterior distribution of the parameters of the sinusoidal model fit to both epochs of data for 2MASS J1047+21 simultaneously. Same as Figure 1C but for a joint analysis of both epochs together. We add an additional parameter to account for the possible evolution of the atmospheric feature and/or differential rotation in the year between epochs. This model favours a rotation period of $1.743^{+0.007}_{-0.008}$ hr.
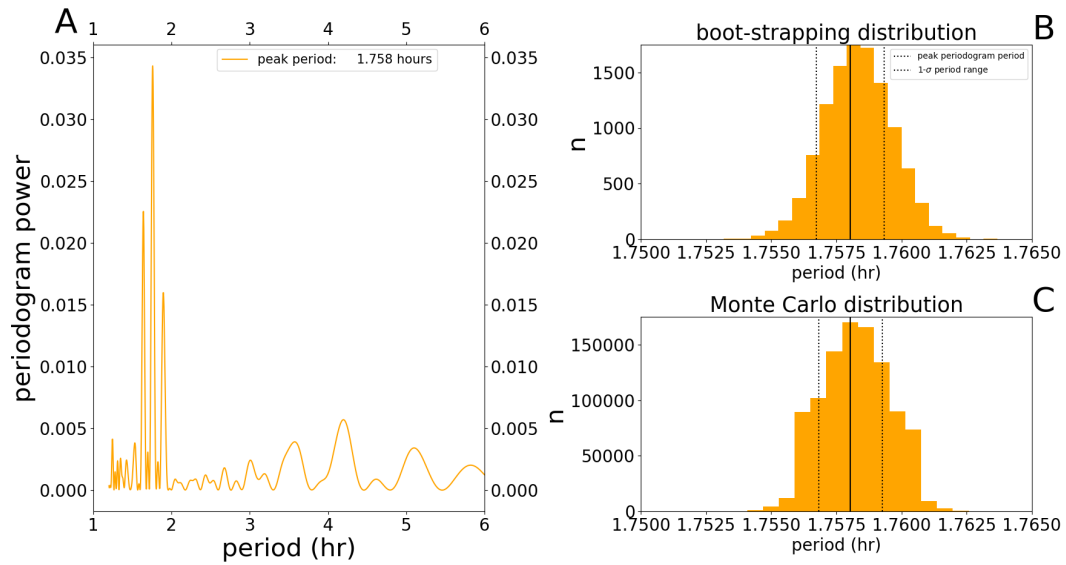
Fig. S6. Lomb-Scargle periodogram and uncertainties for all three nights of VLA data. Same as Figure 2, but for the VLA radio data. The highest power period is 1.758 hours. The two narrow side peaks (A) are aliases resulting from the timing of our observations over three separate nights.